Anatomical correlates of face patches in macaque inferotemporal cortex

Michael J. Arcaro[a,1] , Theodora Mautz[b] , Vladimir K. Berezovskii[b] , and Margaret S. Livingstone[b,1]

[a]Department of Psychology, University of Pennsylvania, Philadelphia, PA 19104; and [b]Department of Neurobiology, Harvard Medical School, Boston, MA 02115

Primate brains typically have regions within the ventral visual stream that are selectively responsive to faces. In macaques, these face patches are located in similar parts of inferotemporal cortex across individuals although correspondence with particular anatomical features has not been reported previously. Here, using high-resolution functional and anatomical imaging, we show that small "bumps," or buried gyri, along the lower bank of the superior temporal sulcus are predictive of the location of face-selective regions. Recordings from implanted multielectrode arrays verified that these bumps contain face-selective neurons. These bumps were present in monkeys raised without seeing faces and that lack face patches, indicating that these anatomical landmarks are predictive of, but not sufficient for, the presence of face selectivity. These bumps are found across primate species that span taxonomy lines, indicating common evolutionary developmental mechanisms. The bumps emerge during fetal development in macaques, indicating that they arise from general developmental mechanisms that result in the regularity of cortical folding of the entire brain.

face patch | cortical folding | structure-function | superior temporal sulcus | macaque

Prior research has demonstrated a relationship between cortical folding and the functional organization of primary sensory areas (1–4). Within the visual system, not only does the calcarine sulcus serve as a macroanatomical landmark for primary visual area V1 (5, 6), but also the folding patterns within the sulcus are predictive of the retinotopic organization (7, 8). Given the complexity and variability in cortical size and shape across individuals, traditionally, it has been thought that there is little correspondence between cortical folding and visual areas beyond V1. However, research over the past decade has revealed a surprising degree of structure-function correspondence across the cortical surface (9–13).

Primates typically have several regions within the inferotemporal cortex (IT) that are selectively responsive to faces. Three spatially distinct sets of face patches—the posterior lateral (PL), middle lateral (ML), and anterior lateral (AL)—have been identified along the lower bank of the superior temporal sulcus (STS) in macaques (14, 15). Two other patches, the middle fundal (MF) and anterior fundal (AF), lie farther down the sulcus at the same anterior-to-posterior (AP) location as ML and AL, respectively. A sixth patch, the anterior middle (AM), is located on the ventral surface of anterior IT. These six face patches are located in similar parts of IT across individuals, although correspondence with particular anatomical features has not been observed previously.

Here, we performed high-resolution anatomical neuroimaging on 18 rhesus macaques. Seven monkeys were raised with normal visual experience of faces and developed face patches identified by functional magnetic resonance imaging (fMRI) within the first year of life. A topological analysis of each monkey's cortical surface revealed that the face patches PL, ML, and AL were localized to focal convex convolutions along the STS, which we refer to as "bumps." These convolutions are morphologically similar to the "buried" or "annectant" gyri previously described

in human and monkey brains, but are probably too subtle to qualify as gyri. Neural recordings from five monkeys confirmed that each bump contained face-selective neurons and demonstrate that targeted recordings of face-selective neurons in the macaque brain can be achieved with high success without requiring fMRI. These bumps were morphologically similar in a separate group of monkeys raised with abnormal visual experiences of faces and that lacked face patches. Thus anatomical landmarks may predict the location of functional specializations but are not sufficient to indicate their presence. Using publicly available datasets, we identified these bumps in utero in rhesus macaques as well as postnatally in several other primate species. This suggests that bump formation emerges from general mechanisms ubiquitous across the primate order. These general mechanisms may underlie the organization of maps, areas, and patterns of architectonics, which in turn may influence functional specializations.

Results

Localization of Face Selectivity to STS Bumps. To probe the relationship between face selectivity and the anatomical topology of IT, we performed functional and anatomical MRI on seven macaque monkeys reared with normal (laboratory) visual experience. Functional scans were aligned to high-resolution (0.5 mm isotropic) T1 anatomical MR images. Regions preferentially responsive to images of faces compared to objects were identified along the lower bank of the STS in the right (Fig. 1) and left

---

Significance

This study reports the discovery that buried gyral folds along the superior temporal sulcus in macaque lateral temporal cortex predict the locations of regions selectively responsive to faces. These findings demonstrate a link between cortical topology and the functional organization of higher-order visual cortex in macaques. We show that these anatomical landmarks are established prenatally and are likely the result of general developmental mechanisms such as molecular signaling gradients, topographic maps, and the formation of cortical areas. These folds are found across primate species. Identification of such anatomical landmarks may provide insight into evolutionary changes in the functional organization of high-level visual cortex.

NEUROSCIENCE

(*SI Appendix,* Fig. S1) hemispheres of each monkey. Face-selective responses covaried with the topology of the STS. The lower bank of the STS is not a uniformly smooth sulcus; rather, there are several focal convolutions along the posterior-to-anterior axis, which we refer to as bumps, where the cortical surface bulges. These bumps are most apparent in parasagittal sections of the STS.

When viewed coronally, the bumps are less prominent relative to the broader convexity of the temporal gyrus. These bumps were visible on both high-resolution T1 images and lower-resolution functional echo-planar imaging (EPI) images (*SI Appendix,* Figs. S2 and S3). Across monkeys, face selectivity consistently fell on three bumps along the posterior-to-anterior extent of the STS,
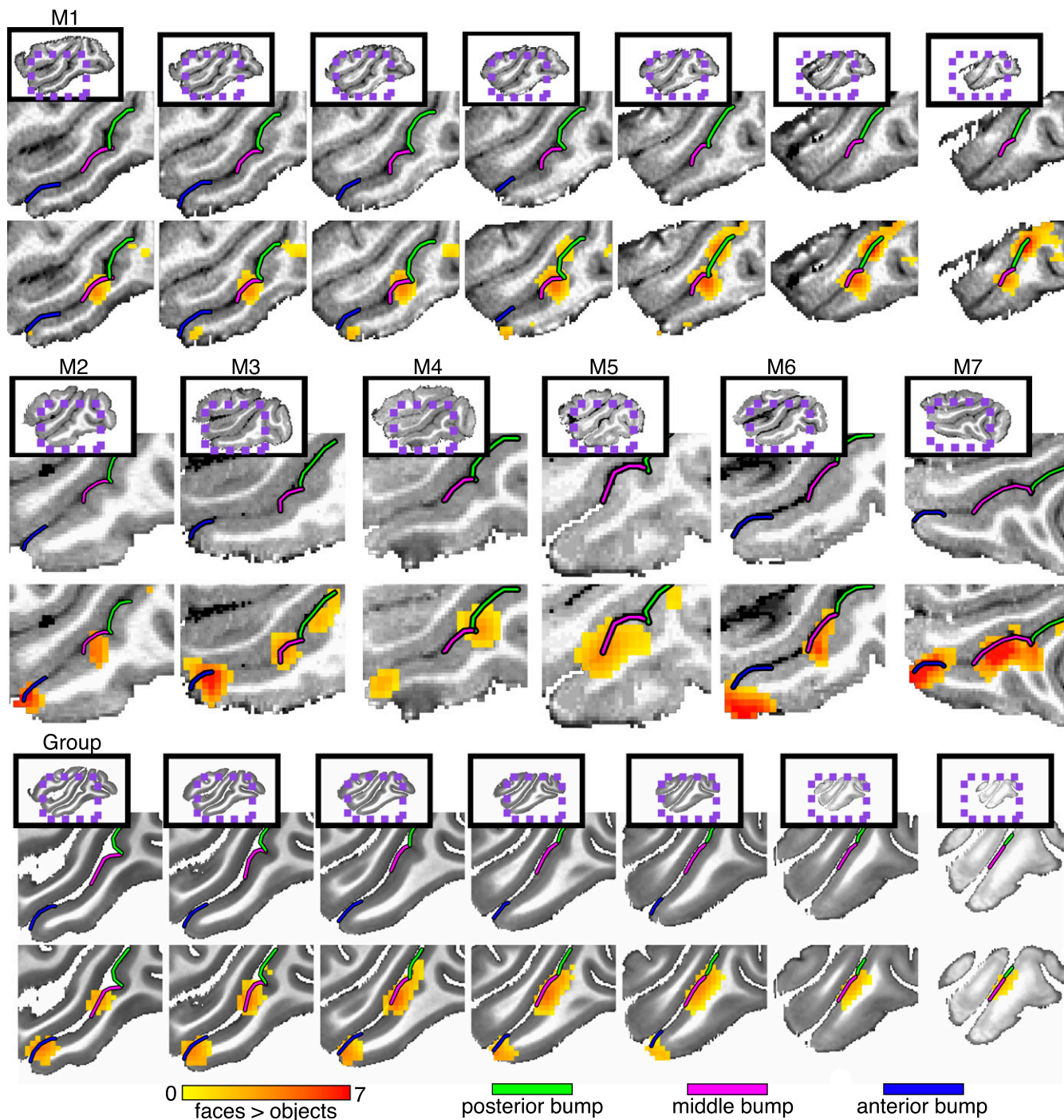

Fig. 1. Anatomical localization of face selectivity in right-hemisphere STS. Preferential activity for faces vs. objects was identified along the lower bank of the STS in all seven monkeys reared with normal face experience (*P* < 0.0001, FDR-corrected). (*Top*) Seven sequential sagittal slices from medial (*Left*) to lateral (*Right*) cortex at 1-mm spacing in the right hemisphere of monkey 1. (*Middle*) Single sagittal slices showing localization of face-selective activity to bumps in the right hemispheres of the other normally reared monkeys. (*Bottom*) Group-average face selectivity falls on anatomical bumps in the STS. Seven sagittal slices from medial (*Left*) to lateral (*Right*) cortex at 1-mm spacing in the right hemisphere of the NMT brain. Group-average faces vs. objects contrast map threshold to show only voxels where at least three monkeys showed significant activity. See *SI Appendix,* Fig. S1, for left-hemisphere counterpart.

which we refer to as the posterior (Fig. 1, green line), middle (pink line), and anterior (blue line) bumps. More broadly, there was no consistent relationship between surface curvature and the magnitude of the response to faces compared to object contrast along the entire STS (t [13] = 2.0268, P = 0.0637). The lack of a positive relationship is likely due to the presence of additional bumps along the STS that are not face selective as well as the prominent mediolateral convexity of the temporal gyrus. Similarly, neither cortical thickness nor sulcal depth were significantly related to face selectivity within the STS (ts [13] < 0.78, ps > 0.45). Together, this indicates that face selectivity was specific to these three anatomical

landmarks and does not reflect a broader relationship between convex cortical folding and face selectivity.

The extent of each bump was identified manually based on cortical curvature (Fig. 2 and *SI Appendix*, Fig. S4). Convexity (curvature) maps were derived from cortical surface reconstructions of the segmented gray matter of T1 images for each monkey. Along the lateral bank of the STS, each bump was constrained laterally by the gyral crown and medially by the fundus. Along the AP axis, each bump was constrained to all adjacent cortex surrounding the peak convexity (highest point of bump; red color in the convexity map) terminating in the local
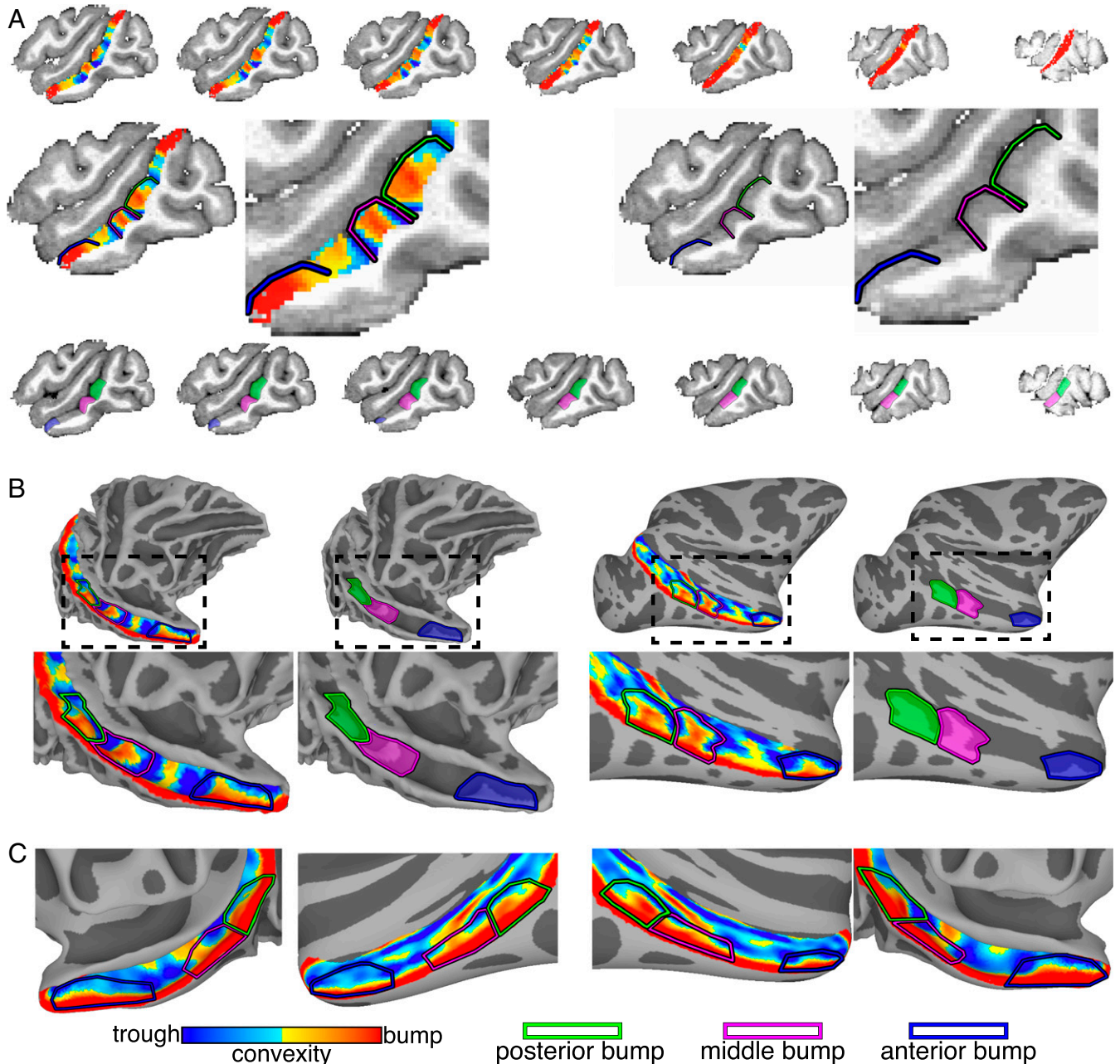
Fig. 2. Identification of STS bumps in each monkey. (*A*) Convexity maps are shown along the lower bank of the STS in seven sagittal slices from medial (*Left*) to lateral (*Right*) (1.5-mm spacing) for the right hemisphere of monkey 2. Enlarged views of single sagittal slices show the bump peaks (red) and troughs (blue). (*B*) Smoothed white matter and inflated cortical-surface reconstructions showing the convexity maps of the STS in the right hemisphere of the same monkey. Posterior (green), middle (pink), and anterior (blue) bumps are shown in both hemispheres. (*C*) Group-average convexity maps with outlines of the three bumps are shown on the right and left hemisphere surfaces of the NMT brain.

Arcaro et al.

minimum (troughs; blue color in the convexity map) of the convexity map (Fig. 2 and *SI Appendix*, Fig. S4). Local troughs surrounding the bumps were clearest within the sulcus of the STS just lateral to the gyral crown. Points near and along the gyral crown had uniformly large positive convexities (red color in the convexity map; Fig. 2 and *SI Appendix*, Fig. S4). In these regions, the boundaries of each bump were identified based on the troughs within the sulcus and the relative low points of the gyral convexity. Across monkeys, the median surface areas for the posterior, middle, and anterior bumps were 83.19 mm^2 (+/− 5.37 SEM), 75.66 mm^2 (+/− 6.81 SEM), and 60.23 mm^2 (+/− 3.32 SEM). The posterior and middle bumps bordered each other in every hemisphere, but there was a gap between the middle and anterior bumps. The AP length of this gap varied across monkeys and always lacked face selectivity (Fig. 1 and *SI Appendix*, Fig. S1). Additional bumps were identified within the STS. In each monkey, one or two bumps were present in the posterior-most part of the STS just anterior to the lunate sulcus where the STS arches superiorly toward the parietal cortex. In a few hemispheres, another small bump was also present between the middle and anterior bumps (e.g., see *SI Appendix*, Fig. S4, monkey 2 [M2]). These additional bumps were not face selective and were not evaluated further.

Along the posterior-anterior axis, the bumps were localized to similar regions of the STS relative to other anatomical folds. The posterior bump (*SI Appendix*, Fig. S4, green outlined region) was localized to where the inferior occipital sulcus (IOS) intersects the STS and just posterior to the posterior middle temporal sulcus (PMTS). The middle bump (pink outlined region) was identified anterior to the posterior bump directly medial and dorsal to the PMTS. The anterior bump (blue outlined region) was found near the anterior tip of the STS directly medial and dorsal to the anterior middle temporal sulcus (AMTS). Across monkeys, the middle bump's surface area tended to scale with the surface area of PMTS ($r = 0.64$, $P < 0.001$), even when controlling for total surface area in each hemisphere (partial correlation: $r = 0.61$, $P < 0.001$), suggesting a relationship between local morphology of the STS and neighboring sulci. However, such a relationship was unclear for the other two bump-sulcal pairs ($rs < 0.28$, $ps > 0.15$).

Face selectivity was strongest and most consistent within the three bumps. Across the cortical surface, the magnitude of face selectivity was strongest in the middle and anterior bumps (Fig. 3, *Top*). Furthermore, face selectivity was most consistently found across monkeys within these bumps as compared to the rest of the STS (and brain for that matter; Fig. 3, *Bottom*). In the right hemisphere, the only regions to show significant face selectivity in each monkey were found along the lateral half of the middle and anterior bumps. In the left hemisphere, the most consistent face selectivity (six of seven monkeys) was found along the lateral side of the middle bump. In general, face selectivity was most consistently found on the lateral half of each bump. Together, these data illustrate a tight correspondence between face selectivity and STS bumps and demonstrate that the most likely cortical location to find face-selective neurons is in the lateral half of the middle and anterior bumps.

Each STS bump corresponded to an individual lateral face patch and was aligned along the AP dimension with fundal face patches. Functional activations were mapped to each monkey's cortical surfaces (*SI Appendix*, Fig. S5), and regions of face selectivity corresponding to previously reported PL, ML, and AL face-selective patches were identified (14, 16, 17). Each face patch was identified in both hemispheres of all monkeys except for AL in the left hemisphere of monkey 2 and PL in the right hemisphere of monkey 4 (*SI Appendix*, Fig. S5). The median surface areas for PL, ML, and AL were 18.78 mm^2 (+/− 3.07 SEM), 48.25 mm^2 (+/− 7.81 SEM), and 33.33 mm^2 (+/− 6.79 SEM). Face-selective regions PL, ML, and AL were localized to
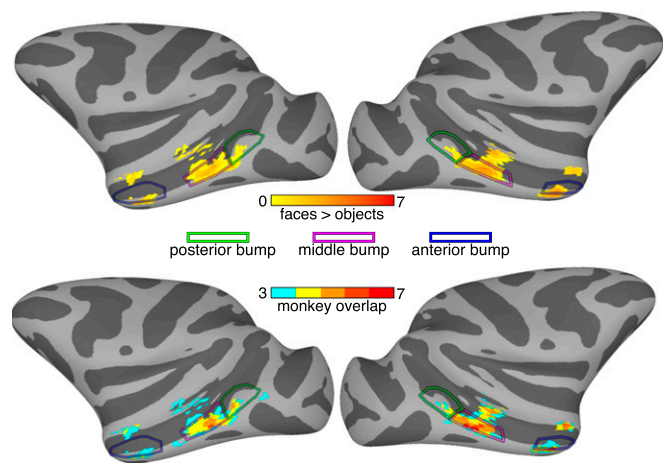

Fig. 3. Localization of face selectivity to STS bumps. (*Top*) Outlines of the three group-average bumps are shown overlaid on group-average face vs. object activations. The group-average map thresholds were set to show only surface nodes where bumps or face selectivity were present in at least three monkeys. Across monkeys, the most face-selective regions along the lower bank of the STS fell within the middle and anterior bumps. (*Bottom*) Outlines of the three group-average bumps are shown overlaid on an overlap map that shows how many monkeys had significant face-selective activity in a given cortical region. Throughout the STS, overlap was strongest in the middle and anterior bumps.

the STS bumps. In both hemispheres of each monkey and in the group average data, PL consistently fell on the posterior bump, ML on the middle bump, and AL on the anterior bump (*SI Appendix*, Fig. S6). Overall spatial correspondence between face regions and STS bumps was quantified by a Dice overlap index that compares the overlap of two regions to their total area and results in values ranging between 0 (no overlap) to 1 (perfect overlap) (Methods – Overlap analysis). For each face patch, a Dice index was calculated with each of the bumps. For PL, ML, and AL, the largest overlap was with the posterior bump (0.31), the middle bump (0.58), and the anterior bump (0.41), respectively (*SI Appendix*, Fig. S6). Although surface area and Dice overlap measures are dependent on the face-localizer threshold, it is clear from these data that 1) face patches were smaller than the bumps, and 2) each face patch covered only a portion of the corresponding bump. Although face patches extended laterally in a few hemispheres across monkeys, each face patch was most consistently localized to the lateral half of the corresponding bump (Fig. 3). Although not previously noted, the localization of PL, ML, and AL face patches to the lateral portions of these bumps is apparent in several prior studies (*SI Appendix*, Fig. S7). Together, these data emphasize a correspondence between each lateral face patch and an individual bump in the STS.

How does knowing the location of these bumps compare with alternative approaches for localizing face patches? When functional mapping is not an option, the alternative gold standard for localizing a functional region is to use a probabilistic atlas where the predicted location of an area is calculated from a separate group of individuals. For each monkey, we created probabilistic atlases of each face patch in both hemispheres using the remaining six monkeys. Consistent with prior work (18), the probabilistic map for each face patch fell within a focal region of the STS. However, there was variability in the spatial overlap of any two monkeys' face patches. For example, when projected onto the National Institute of Mental Health macaque template (NMT) brain, the entire right ML face patch of monkey 5 fell anterior to the ML face patch of monkey 4. This spatial offset along the AP axis mirrored monkey 5's middle bump falling anterior to monkey 4's middle bump on the NMT brain.

At a finer scale, variability in where ML fell on the middle bump was apparent when looking at face selectivity on the native EPI images of individual monkeys (*SI Appendix*, Figs. S2 and S3). ML falls on the anterior part of monkey 5's middle bump, but on the posterior part of monkey 4's middle bump. Furthermore, few (or no) parts of each probabilistic face patch had 100% overlap across monkeys. On average, the overlap between any individual monkey's face patch and the corresponding probabilistic atlas (*SI Appendix*, Fig. S8; PL, ML, and AL Dice indices = 0.30, 0.46, 0.35, respectively) was worse than the overlap of individual bumps and face patches (*SI Appendix*, Fig. S6). Thus, while probabilistic atlases are useful, similar to the bumps, such approaches are also imperfect at predicting the location of face regions in an individual subject. To directly compare the predictability of bumps with functional atlases, we evaluated the distances between the centroids of each face patch and its corresponding bump/probabilistic map. Although each face patch at least partially overlapped the corresponding bump, a centroid analysis provides additional information on how well aligned these regions are. The centroids of face patches were clustered near the centroid of corresponding bumps, particularly along the AP axis, although most face patch centroids fell closer in the medial-to-lateral axis to the gyral crown of the STS's lower bank than the bump centroids (Fig. 4, *Top*). Consistent with the Dice overlap analysis, the distance along the cortical surface was shortest between each face-patch centroid and the centroid of the corresponding bump (PL and posterior bump = 4.28 mm; ML and the middle bump = 2.72 mm; AL and the anterior bump = 5.42 mm). Furthermore, for each face patch, the variance in centroid distances across monkeys was smallest for the corresponding bumps. This indicates that each bump was not just the closest anatomical landmark for its corresponding face patch but also the most predictive of the face patch's location. Across monkeys, the overlap was highest and the centroid distances
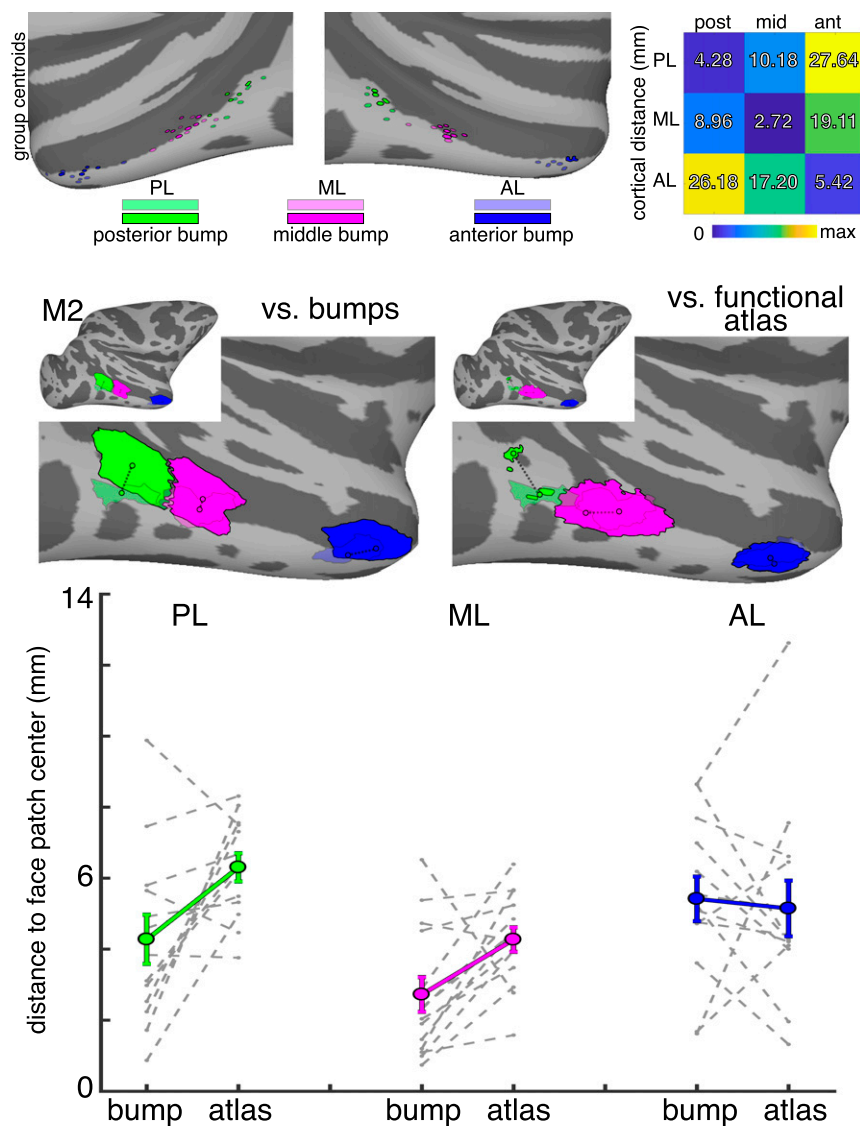
Fig. 4. Distances between face regions and STS bumps. (*Top*) The centroids of all monkeys' face regions and bumps are shown on the NMT brain surface. The group mean distances along the cortical surface (in mm) are shown for all face patch x bump comparisons. (*Middle*, *Left*) The distances between the centroids of each face patch and the corresponding bumps are shown for monkey 2. (*Middle*, *Right*) The distances between the centroids of each face patch and probabilistic functional atlases for each face patch (from a separate group of monkeys) are shown for monkey 2. (*Bottom*) The distances between bump centroids and face regions and the distances between the probabilistic functional atlas centroids and face regions are shown for individual monkeys (gray dashed lines) and group average (solid colored lines) in PL, ML, and AL.

Arcaro et al.

were shortest between the ML face patch and middle STS bump, indicating that this pair had the strongest structure-function correspondence of the three lateral face regions. The distances between the posterior bump and PL tended to be smaller than the distances between the probabilistic PL and individual monkey's PL (Fig. 4, *Bottom*; t [12] = −2.93, P = 0.0127). Similarly, the distances between the middle bump and ML tended to be smaller than the distances between the probabilistic ML and individual monkey's ML (t [13] = −3.16, P = 0.0076). There were minimal differences in these distances for AL (t [13] = 0.43, P = 0.68). Overall, this suggests that identifying the location of these bumps is comparable to, and in most cases better than, probabilistic atlases.

Using Bumps to Target Neural Recordings. Each bump contained face-selective neurons. We performed computed tomography (CT) imaging to anatomically target multielectrode array implantation along the lower bank of the STS in five monkeys. Each array was successfully implanted within one of the STS bumps. In each monkey, the vast majority of channels were selectively responsive to faces vs. hands, bodies, and inanimate objects (Fig. 5 and *SI Appendix*, Fig. S9). Although we used fMRI in each monkey to verify that face selectivity fell on bumps, we used the bumps as anatomical markers during surgery for our array implantation. Given that the centroids of each face patch tended to fall on the lateral extent of each bump (Fig. 4 and *SI Appendix*, Fig. S6), we targeted the lateral half of each bump just below the gyral crown of the lower bank of the STS for implantation. The long dimension of each PL and ML array was oriented posterior-to-anterior along the STS and covered the majority of each bump. Furthermore, all arrays targeting face-selective regions have been within bumps, and we have yet to implant an array into a bump and not find the majority of channels to be face selective. Acute recordings from single-electrode penetrations should also benefit from targeting the bumps as a chamber centered on a bump will guarantee coverage of the corresponding face patch, although multiple penetrations may be required. Together, this indicates that the bumps are sufficient for targeting recordings from face-selective neurons.

Anatomical Landmarks Are Not Sufficient for Face Selectivity. Although the location of face patches can be predicted by the STS bumps, this anatomical feature of the STS does not necessarily indicate the presence of face selectivity. We collected high-resolution T1 anatomical images in seven monkeys with abnormal early visual experience of faces. Four of these monkeys were raised without seeing faces for the first year of life and did not develop face patches (three of these monkeys were originally reported in ref. 19). Two other monkeys were raised under conditions of binocular visual form deprivation (not specific to faces) for the first year of life and also did not develop face patches. The seventh monkey was raised in an environment where he had excess exposure of faces to his peripheral visual field during early development (in contrast to the typical foveally biased visual experience of faces). Although this monkey saw faces and developed face patches, his experience was atypical and serves as a test case for whether the type of face experience affects bump anatomy. In each monkey, the posterior, middle, and anterior bumps were present despite abnormal early face
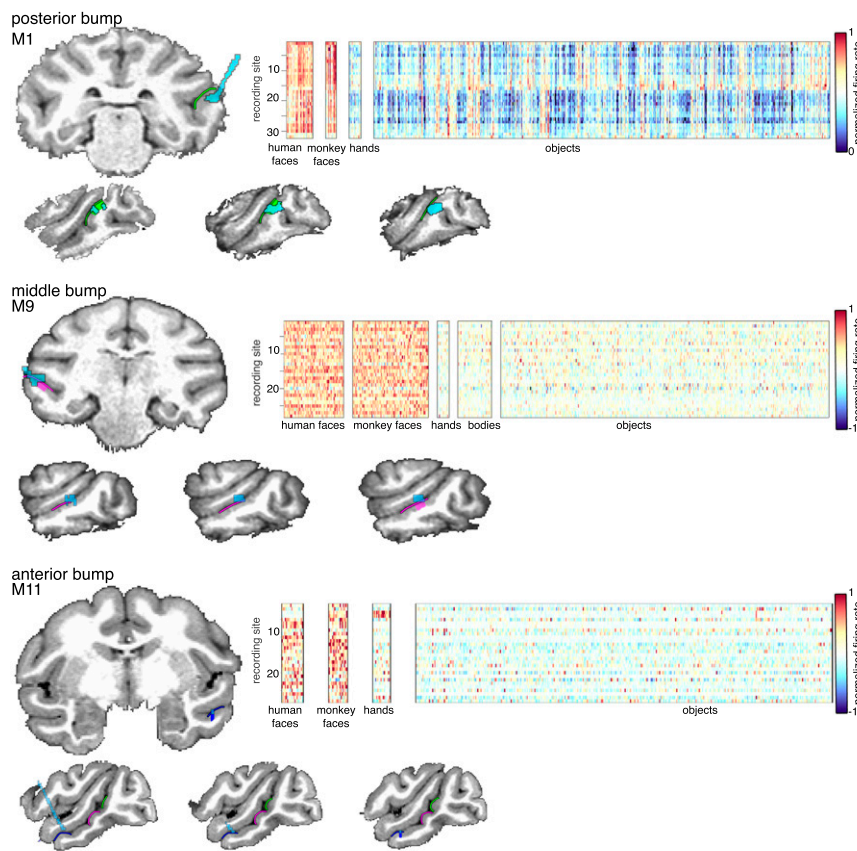
Fig. 5. Multielectrode recordings from STS bumps. Multielectrode arrays were implanted in the posterior, middle, and anterior bumps of three macaque monkeys. In each array, the majority of channels were selectively responsive to human and monkey faces vs. hands, bodies, and inanimate objects. In each brain, the array base and wires from CT imaging are in blue. See *SI Appendix*, Fig. S9, for additional monkeys/arrays.

experience (*SI Appendix*, Figs. S10 and S11). Relative to nearby anatomical landmarks such as the IOS, PMTS, and AMTS, the bumps were in similar parts of the STS as compared to the seven control monkeys reared with normal face experience. Furthermore, the group average bumps from this abnormal monkey group were in good spatial correspondence with the group average bumps from control monkeys (*SI Appendix*, Fig. S12). There was a high degree of Dice overlap in the extent of the posterior (0.81), middle (0.73), and anterior (0.77) bumps between the two monkey groups. The distances between the centroids of the posterior (2.42 mm +/− 0.44), middle (2.17 mm +/− 0.37), and anterior (2.01 mm +/− 0.56) bumps in each monkey with abnormal early visual experience and the mean centroids in the control group were, on average, within a few millimeters of each other. The distances between centroids of each bump in the abnormal early visual experience group and centroids of the probabilistic face patches were comparable to the centroid distances between bumps and face patches in normally reared individuals (*SI Appendix*, Fig. S12, *Right*), demonstrating that these bumps are useful for targeting regions of the STS where face patches normally develop such as in baby monkeys younger than 6 mo (20) and in monkeys raised without seeing faces (19). The Dice overlap and centroid distances were comparable between the following three subgroups of abnormal monkeys: 1) monkeys raised without seeing faces, 2) monkeys raised with a binocular visual form deprivation, and 3) monkeys raised with abnormal constant exposure to faces across the visual field (*SI Appendix*, Fig. S13). The only anatomical difference found between the control and abnormal monkey groups was cortical thickness. The average cortical thickness was greater in control monkeys for the posterior (1.97 +/− 0.03 vs. 1.87 +/− 0.05), middle (2.15 +/− 0.03 vs. 1.97 +/− 0.05), and anterior (2.10 +/− 0.02 vs. 1.95 +/− 0.04) bumps. These small differences were likely due to the abnormal monkey group being younger on average (1.43 +/− 0.24 y old) than the control monkey group (3.51 +/− 1.5 y old). Together, these data suggest that the STS bumps are present in individuals that lack face selectivity and that their macroanatomical organization is similar to that found in monkeys that have face patches.

Developmental and Evolutionary Origins of STS Bumps. STS bumps appear prenatally and are evolutionarily preserved across primate species. Although the STS bumps are not clearly formed by gestation day (GD) 110 the sulcus has already begun to bend near where bumps emerge (Fig. 6*A*; black dashed circle). By GD 135, the posterior, middle, and anterior bumps are all present (Fig. 6*A*, green, pink, and blue arrows); this is after the cortical plate has formed and the geniculate has innervated visual cortex (21). Thus, the bumps emerge prior to seeing faces and well before the development of face patches. The presence of these bumps in utero indicates that they form from general principles of cortical folding and cortical expansion. Do these bumps manifest in other primate species? Despite the cortical surface in New World Monkeys being relatively lissencephalic and lacking substantial folds, capuchins have a prominent bump along the middle of their STS anterior to their IOS (Fig. 6*B*). Similar to rhesus macaques, other Old World monkeys including mangabeys and cynomolgus macaques also have clear posterior, middle, and anterior bumps along their STSs. Gibbons and baboons also have similar bumps. Although the cortical surface is much larger in Great Apes and ape brains contain substantially more folds than macaques, gorillas have at least posterior and middle bumps in similar parts of their STS. The topology of the STS is more complex in orangutans, chimps, and humans, and several bumps are apparent. In humans, these bumps likely correspond to several buried annectant gyri called "plis de passage" (22). It is unclear which, if any, of these small gyri correspond to the three

bumps in macaques and whether these human folds contain functional specializations such as face selectivity.

Discussion

Our results show a correspondence between the locations of face patches and focal convolutions, which we refer to as bumps, along the surface of macaque STS. In each monkey, we identified three prominent bumps: posterior, middle, and anterior bumps that correspond to the fMRI-defined PL, ML, and AL face patches, respectively. Previous research has shown that these face patches fall within similar regions of the STS across individuals (18), but correspondence with specific anatomical landmarks has not been reported. Here, we show that the most probable cortical locations of face-selective activity are within these bumps. Our analyses indicate that using the bumps to localize face patches is superior to using a functionally defined probabilistic atlas derived from a separate group of monkeys. Furthermore, recordings from implanted arrays confirmed the prevalence of face-selective neurons within each bump. Together, we demonstrate a way to target face patches in the macaque brain based solely on anatomy.

The bumps are stable macroanatomical landmarks for identifying the location of face-selective neurons. These findings provide insight into the relationship between cortical topology and the functional organization of higher-order visual cortex (9, 23–25). Recent research has shown that local sulcal features can predict the location of functional domains in the human ventral temporal cortex (11, 26, 27). Specifically, the anterior tip of the midfusiform sulcus is predictive of the location of face-selective area FFA-2. From this work, one might assume that macaques also would have an anatomical landmark for face patches. However, the sulcal and gyral topology of the face-selective cortex differs substantially between humans and macaques. Macaques lack a fusiform cortex, and the putative homologous face-selective patches are found in an entirely different sulcus, the STS (15). Thus, it is unclear whether and how such correspondences would hold across these two species. Furthermore, here we find that face patches are anchored to convex bumps, not sulci. Thus, face patches map to particular anatomical features in both primate species, but the specific landmark and even the general property of cortical folding (convex vs. concave) differ. This is particularly notable since sulcal and gyral regions are hypothesized to differ in their myeloarchitecture (28) and areal connectivity (29) and, by extension, their functional properties (30). The identification of these structure-function correspondences in multiple species provides insight for testing the functional correlates of cortical folding.

Our results add to a growing body of literature characterizing the morphological features of cortical folding including sulcal pits and annectant gyri (10, 22, 31, 32). Although less studied in Old Word monkeys, such features are associated with functional specializations in humans (31, 33–35). Of particular note, several plis de passage (annectant gyri) in the human STS are thought to reflect distinct structural connectivity bridging superior and middle temporal gyri and functional specializations (35–37). Similar to these plis de passages, the macaque STS bumps 1) are convolutions buried in the main furrow of the STS, 2) are distributed along the posterior-to-anterior axis, 3) are consistent in their location across individuals, and 4) emerge early in development. However, there are notable differences. Superficial human plis de passages typically span both sulcal banks and form a clear interruption of the sulcus. In contrast, the middle and anterior macaque STS bumps extend into the fundus but are not contiguous with convolutions along the upper bank of the STS in most hemispheres. This discontinuity may be similar to "deep" plis de passages reported recently in the human STS that are partially disconnected in the fundus (36). A continuous bump extending to the upper bank was apparent only for the middle
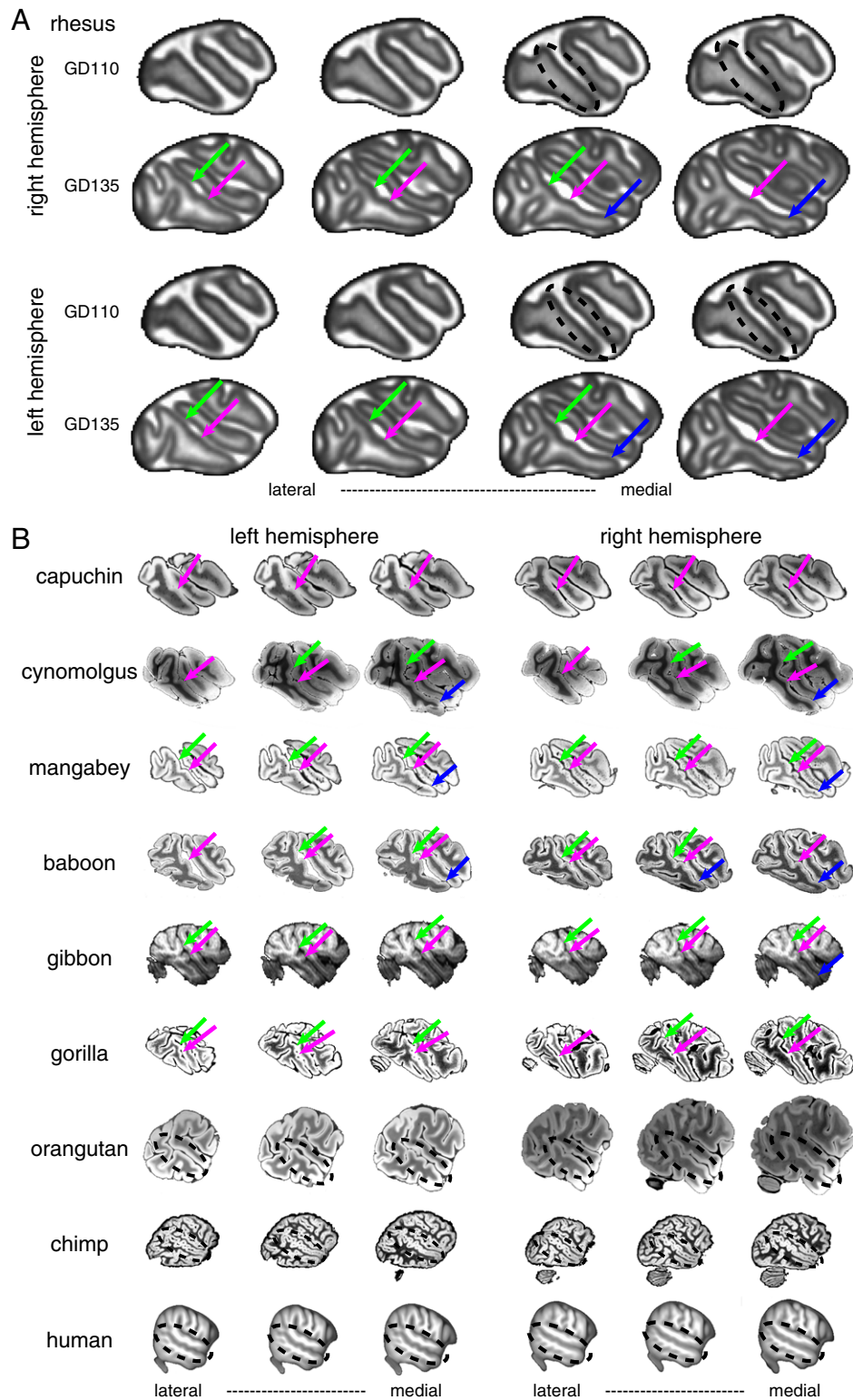
Fig. 6. Bump phylogeny and ontogeny. (*A*) The bump appears early in development. The bumps are not clearly identifiable at GD 110 but are present by GD 135. Green, pink, and blue arrows indicate posterior, middle, and anterior regions of the STS with bumps. MRI images are part of the Oregon National Primate Research Center Fetal Macaque Brain Atlas. (*B*) Bumps along the STS are present in several primate species spanning New World Monkeys, Old World Monkeys, gibbons, and baboons. The gorilla STS has bumps similar to macaques, but all other Great Apes have a more complicated folding structure with several bumps along the STS. All MRI images except for the gibbons come from T2W scans. Gibbons are from T1 scans. Dashed circle shows the STS in Great Apes. Gibbon MRI data are taken from the National Chimpanzee Brain Database (https://braincatalogue.org/). Human MRI data are taken from the T1 group average from the HCP 1200 Young Adult dataset (https://www.humanconnectome.org/study/hcp-young-adult). All other MRI data are taken from the Brain Catalogue (https://braincatalogue.org/).

bump and only in 3 of 14 hemispheres in our control group. Although anatomical connections exist between face patches along the lower and upper banks of the STS (38), the correspondence of these tracts to the convolutions of the STS remain to be resolved. Instead of being homologous to the human STS, the macaque bumps may correspond to convolutions along the fusiform gyrus where putatively homologous face patches exist. Although annectant gyri have not been documented for human face patches along the fusiform, the morphology of a plis de passage in the visual word form area along the fusiform has been shown to be correlated with reading skills (39).

What is the possible developmental relationship between the three bumps distributed along the STS and face patches? A consistent structure–function relationship could be taken as evidence that the location where face patches develop in IT is predetermined and that the bumps represent circuitry genetically specialized for processing faces. However, morphologically similar bumps were apparent in monkeys that lacked face patches, demonstrating that STS bumps are not sufficient to produce face selectivity in the absence of face experience. Furthermore, these bumps are present in utero prior to the onset of vision, and face patches do not appear until 200 d of age (20). The prenatal formation of these bumps and the consistency in their anatomical location across individuals are doubtless the result of the same general developmental mechanisms that result in the regularity of cortical folding of the entire brain. These factors must include molecular signaling gradients that can indirectly influence folding by limiting the expandability, stiffness, or thickness of the cortical surface (40) and mechanical pressures such as axonal tension (29) or differential growth rates of superficial and deep cortical layers (41–43). In particular, regionally specific growth applied to a species-specific initial geometry may suffice for producing species-specific folds (44). The presence of these bumps in late stages of gestation prior to visual experience is consistent with recent observations that gyri form only after the completion of neurogenesis and are driven by the rapid growth of intracortical neuropil and the enlargement of subjacent white matter consisting of cortio-cortical connections (32). Together,

our data provide additional support for the protomap hypothesis (33), which postulates that intrinsic patterning mechanisms establish the initial arealization of cerebral cortex. Given that sulcal and gyral regions are hypothesized to differ in their laminar architecture (28) and areal connectivity (29), these bumps comprise part of the early cortical architecture that constrains and guides postnatal development.

The precise location where each face patch fell on a given bump varied across individuals. Face patches typically fell on the lateral half of the bumps although face-selective activity was found medial to the lateral patches (Fig. 2) and likely corresponds to the MF and AF face patches. More notably, face patches varied in their localization along the AP axis of the bumps. This variability was evident in the EPI images (*SI Appendix*, Figs. S2 and S3) and thus cannot be attributed to misalignment with the high-resolution anatomical images. It is also unlikely that any differences in vasculature across individuals could account for such variability since the peak of face-selective fMRI activity corresponds to the highest concentration of face-selective neurons (16, 45). Instead, this likely reflects true variability in the precise anatomical location of face patches on bumps across individuals. Given that face-patch development depends on face experience (19) and adheres to a retinotopic proto-organization across IT (46), such local variability may simply reflect idiosyncrasies of each monkey's visual experience with faces and how it mapped onto an intrinsic functional architecture. Indeed, a recent study in humans showed a correspondence between individual face-viewing behavior and the receptive field properties of face-selective regions (47). It remains to be seen whether macaque STS bumps undergo morphological changes across postnatal development and if such changes have any relationship to functional maturation. Thus, it is plausible to have a consistent structure–function correspondence across individuals where the presence and precise localization of function is dependent on how experience interacts with an intrinsic architecture.

Is there a mechanistic explanation for the association between face patches and bumps? Like Gaul, inferotemporal cortex is
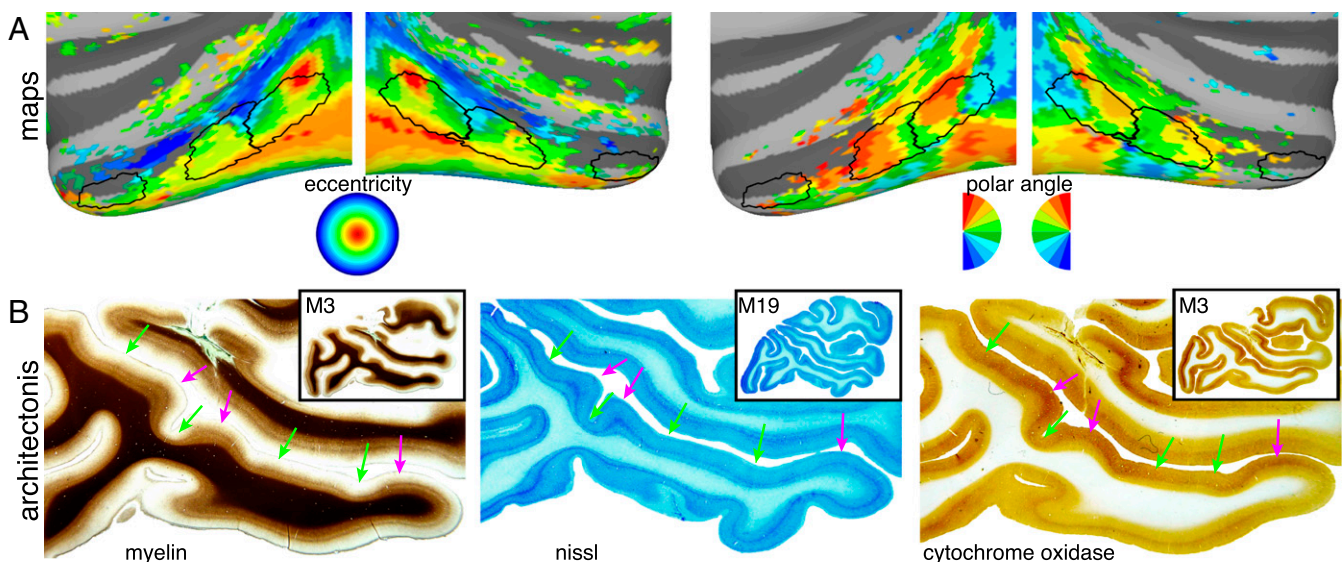
Fig. 7. Relationship of bumps to functional maps and architectonics. (*A*) Correspondence between STS bumps and retinotopic organization in IT. (*Left*) Outlines of the STS bumps are shown overlaid on eccentricity maps covering the central 10 degrees of visual space that differentiate representations of central (red/yellow) and peripheral (blue) visual space. (*Right*) Outlines of the STS bumps are overlaid on polar angle maps of visual space that differentiate representations of upper (red), horizontal (green), and lower (blue) meridian representations. (*B*) Architectonic features that vary along the STS. Low-magnification (12×) images of sagittal sections through the STS. The degree of (*Left*) myelination, (*Middle*) Nissl, and (*Right*) cytochrome oxidase staining varies within and around the STS bumps. See *SI Appendix*, Figs. S14 and S15, for examples from additional monkeys. Pink arrows illustrate the three bumps that show darker staining for both myelin and cytochrome oxidase. Green arrows indicate neighboring nonbump regions of the STS with lighter staining.

generally divided into three parts: anterior (AIT), middle (CIT), and posterior (PIT). Retinotopic mapping shows several central-visual-field foci along the lower bank of the STS with repeating representations of polar angle indicating the presence of multiple visual maps across these three parts of IT (Fig. 7*A*) (48). Along the STS, there are three sets of face patches, adjacent sets of body patches (16, 17, 49, 50), and three sets of color patches similarly distributed along the STS (15, 17, 51). Thus, the three bumps reflect some aspect of arealization with a complement of retinotopy and functionality in each area. Whether folding dictates arealization or the reverse is unknown, although prominent cortical folds demarcate the borders between multiple early visual areas (1). Cortical folding applies mechanical pressures that affect laminar morphology (52, 53). Indeed, the laminar organization of the bumps differs relative to the surrounding STS. Bumps appear to have 1) greater cortical thickness, 2) staining for myelin in superficial layers (Fig. 7*B* and *SI Appendix*, Fig. S14), 3) thick deep (V and VI) layers (Fig. 7*B* and *SI Appendix*, Fig. S12, Nissl stains), and 4) strong staining for cytochrome oxidase (Fig. 7*B* and *SI Appendix*, Fig. S15). These observations are consistent with prior reports of laminar differences between gyri and sulci across cortex (52, 54) and may have a substantial influence on functional properties (52). It has been hypothesized that areal connectivity varies systematically with cortical folding. Axonal connections in cortical folds tend to be short and straight, connecting adjacent gyral walls (29, 54). The association of face patches, and central visual-field representation, with the development of convex bumps is particularly notable given theories of gyrogenesis (34), which propose a correspondence between sulcal folds and cytoarchitectonic boundaries, thereby potentially centering functional areas on gyri (23). The bumps may be related to a relative expansion of the central visual field. It is also possible that the neuronal morphology and connectivity within these bumps may support computations particularly well-suited for the processing of high-resolution vision in general and faces in particular.

It remains to be seen whether the presence of STS bumps in other animal species indicates the existence or location of face patches, and/or expanded central-visual-field representations. The structure-function topology of visual cortex substantially differs between humans and Old World monkeys. It is generally thought that the face patches within the STS of rhesus macaques correspond functionally to the face patches within and around the fusiform cortex of humans (15). Although humans also have face-selective regions in their STS (17), these areas differ in their response properties from the human fusiform areas and are associated more with social and affect features of face processing (55, 56). The prominence of these bumps does not fall along strict taxonomy lines, as corresponding bumps were prominent in gorillas but less so in other apes. Identification of such anatomical landmarks may provide insight into evolutionary changes in the functional organization of high-level visual cortex.

Materials and Methods

Monkeys. Functional and anatomical MRI studies were carried out on 24 Macaca mulatta, 5 female and 19 male. All procedures were approved by the Harvard Medical School Animal Care and Use Committee and conformed with NIH guidelines for the humane care and use of laboratory animals. Seventeen monkeys (M1–M11, M19–M24) were cohoused with their mothers in a room with other monkeys for the first several months and then cohoused with other juveniles, also in a room with other monkeys. Seven of these monkeys (M1–M7) participated in both anatomical and functional neuroimaging experiments. Monkey 1 and the other four monkeys (M8–M11) participated in anatomical imaging and electrophysiological recordings from chronically implanted multielectrode arrays. As part of separate experiments, seven monkeys (M12–M18) were raised with abnormal visual experience of faces. Six of these monkeys (M12–M17) were hand reared by humans for the first year and then were cohoused with other juveniles. Four of the hand-reared monkeys (M12, M13, M16, M17) were raised by laboratory staff

wearing welders' masks that prevented the monkey from seeing the staff member's face. The only visual experience that they had with faces of any kind were during experiments, which constituted at most 2 h per week, with the face exposure being a minor fraction of that time. The other two hand-reared monkeys (M14 and M15) were raised under conditions of binocular-visual-form deprivation via eye lid suturing for the first year. Finally, one monkey (M18) was raised with his mother in an environment with large posters of faces on the walls such that he had an abnormal, constant exposure to faces in his peripheral visual field. As previously reported (57), for functional imaging, monkeys were alert, and their heads were immobilized using a foam-padded helmet with a chinstrap that delivered juice. The monkeys were scanned in a primate chair that allowed them to move their bodies and limbs freely, but their heads were restrained in a forward-looking position by the padded helmet. The monkeys were rewarded with juice for maintaining a central fixation within a 2° window. Gaze direction was monitored using an infrared eye tracker (ISCAN).

Electrode Implantation. Multielectrode arrays were implanted within the STS of five male Macaca mulatta. Each array was implanted to target face-selective patches. In monkey 1, a floating microelectrode array (FMA) (32-channel Microprobes FMA; https://microprobes.com/products/multichannel-arrays/fma) was implanted within the middle of the posterior bump of the STS corresponding to his PL face patch. The internal dimensions of the FMA array was 3.5 × 1.5 mm with a spacing of 370 to 400 μm between electrodes (across the width and length of the array, respectively). In monkey 8, two FMAs were implanted in the left hemisphere—one within the anterior part of the posterior bump corresponding to his PL face patch and a second array within the anterior part of the middle bump corresponding to his ML face patch. In monkey 9, one FMA was implanted in the left hemisphere centrally within the middle bump corresponding to his ML face patch. In monkey 10, one FMA was implanted within the anterior part of the middle bump corresponding to his ML patch. In monkey 11, a 64-channel 12.5-μm NiCr microwire array (58) was implanted centrally within the anterior bump corresponding to his AL face patch. Monkeys were trained to perform a fixation task. Neural recordings were performed on a 64-channel Plexon Omniplex Acquisition System.

Electrophysiology Display. We used MonkeyLogic to control experimental workflow (https://monkeylogic.nimh.nih.gov). Visual stimuli were displayed on a 19-inch Dell LCD screen monitor with a 60-Hz refresh rate and a 4:3 aspect ratio positioned 54 cm in front of each monkey.

Anatomical Imaging. As previously reported (57), a whole-brain structural volume was acquired while the animals were anesthetized with a combination of Ketamine (4 mg/kg) and Dexdomitor (0.02 mg/kg). Scans were acquired in each monkey using a 3 T Siemens Skyra, using a 15-channel transmit/receive knee coil. Monkeys were scanned using a magnetization-prepared rapid gradient echo (MPRAGE) sequence; $0.5 \times 0.5 \times 0.5$ resolution; field of view = 128 mm; 256×256 matrix; repetition time (TR) = 2,700 ms; echo time (TE) = 3.35 ms; inversion time (TI) = 859 ms; flip angle = 9°. Three whole-brain T1-weighted anatomical images were collected from each animal.

Reconstruction of cortical surfaces. Each animal's T$_1$ images were coregistered to derive an average anatomical volume image for each monkey. Each monkey's average anatomical volume underwent semiautomated cortical surface reconstruction using FreeSurfer. To ensure high accuracy, skull stripping and white-matter masks were first manually segmented by an expert slice-by-slice along coronal, axial, and sagittal planes and then passed into FreeSurfer's autorecon pipeline. Pial and white-matter surfaces were inspected to ensure accurate segmentation. If poor segmentations were detected, the white-matter mask and control points were edited, and surface reconstruction was rerun until corrected. For several monkeys, FreeSurfer's autosegmentation had trouble with the calcarine and highly vascularized regions such as the insula. To fix these segmentation errors, average anatomical volumes were manually edited to improve the gray/white-matter contrasts and remove surrounding nonbrain structures (e.g., sinuses, arachnoid, and dura matter).

Generation of anatomical feature maps. For each monkey, Freesurfer's automated algorithm was used to obtain sulcal depth and convexity maps for the pial and white-matter surfaces. Sulcal depth (in mm) is measured as the distance between the inflated surface and pial surface (59) at each vertex. Convexity maps along the pial and white-matter surfaces were obtained using Analysis of Functional NeuroImages (AFNI)/SUMA's automated algorithm (part of SurfaceMetrics). The pial and smooth white-matter convexity maps were averaged to produce a mean convexity map.

Stimuli. Visual stimuli were projected onto a screen at the end of the scanner bore.

Static images. Responses to image categories of faces and inanimate objects were probed as previously reported (57). Each scan was composed of blocks of each image category; each image subtended 20 ° × 20 ° of the visual angle and was presented for 0.5 s; block length was 20 s, with 20 s of a neutral gray screen between image blocks. Blocks and images were presented in a counterbalanced order. All images were centered on a pink noise background. All images were equated for spatial frequency and luminance using the SHINE toolbox (60).

Functional Imaging. As previously reported (57), monkeys were scanned in a 3-T TimTrio scanner with an AC88 gradient insert using four-channel surface coils (custom made by Azma Maryam at the Martinos Imaging Center, Charlestown, MA). Each scan session consisted of 10 or more functional scans. We used a TR of 2 s, TE of 13 ms, flip angle of 72 °, integrated parallel acquisition techniques = 2, 1-mm isotropic voxels, matrix size 96 × 96 mm, and 67 contiguous sagittal slices. To enhance contrast (61, 62), we injected 12 mg/kg monocrystalline iron oxide nanoparticles (Feraheme, AMAG Pharmaceuticals) in the saphenous vein just before scanning.

General fMRI Preprocessing. As previously reported (57), functional scan data were analyzed using AFNI (Research Resource Identifier [RRID]: nif-0000-00259) (63), SUMA (64), Freesurfer (RRID:nif-0000-00304) (65, 66), JIP Analysis Toolkit (67), and MATLAB (Mathworks, RRID:nlx_153890). Each scan session for each monkey was analyzed separately. Using AFNI, all images from each scan session were aligned to a single time point for that session, detrended, and motion corrected. Data were spatially filtered using a Gaussian filter of 2 mm full width at half-maximum to increase the signal-to-noise ratio while preserving spatial specificity. Each scan was normalized to its mean. Data were registered using a two-step linear and then a nonlinear alignment approach (JIP Analysis Toolkit) to a high-resolution (0.5 mm) anatomical image for each monkey. First, a 12-parameter linear registration was performed between the mean EPI image for a given session and a high-resolution anatomical image. Next, a nonlinear, diffeomorphic registration was conducted. To improve registration accuracy of the ventral cortex, we manually drew masks that excluded the cerebellum for both EPI and anatomical volumes prior to registration.

fMRI Stimulus Category Analysis. As previously reported (57), a multiple regression analysis [AFNI's 3dDeconvolve (63)] in the framework of a general linear model was performed on the category experiments for each monkey separately. Each stimulus condition was modeled with a MION-based hemodynamic response function (61). Additional regressors that accounted for variance due to baseline shifts between time series, linear drifts, and head-motion-parameter estimates were also included in the regression model. Due to the time-course normalization, beta coefficients were scaled to reflect the percentage of signal change. Since MION inverts the signal, the sign of beta values were inverted to follow normal fMRI conventions of increased activity being represented by positive values. Brain regions that responded more strongly to monkey faces than familiar objects were identified by contrasting presentation blocks of each of these image categories. Maps of beta coefficients were clustered (>10 adjacent voxels), and the threshold was at $P < 0.0001$ (false discovery rate [FDR]-corrected).

Lateral Face-Patch Identification. Functional activations were mapped to each monkey's cortical surfaces (*SI Appendix*, Fig. S5), and regions of face selectivity along the lower bank of the STS corresponding to previously reported PL, ML, and AL face-selective patches were identified (14, 16, 17). In some monkeys, face-selective activity extended medially into what were likely the fundal face patches (e.g., ML and MF in monkey 7, *SI Appendix*, Fig. S5). For these cases, the border between adjacent face patches was identified as a trough in the gradient of face selectivity.

Anatomical Analyses. Surface area (in square millimeters) was estimated along the pial surface using AFNI's SurfMeasures. Distances between surface nodes were calculated along the cortical surface using AFNI's SurfDist.

Overlap Analysis. Spatial correspondence between cortical areas was assessed using the Sorensen-Dice coefficient metric ($2|ROI1 \cap ROI2|/[|ROI1| + |ROI2|]$).

Group Analyses. To directly compare functional data across monkeys, each monkey's activation maps were aligned to a standard template surface (NMT) using surface-based registration (Freesurfer/SUMA). After projecting individual subject data to the template, faces vs. objects contrast maps were averaged across monkeys to yield a group average beta map. To visualize group average face selectivity, the data were threshold such that any given surface node needed to show significantly greater activity to faces vs. objects ($P < 0.0001$, FDR-corrected) in at least three of seven monkeys. To create group average region-of-interest (ROI) masks for face-selective regions and anatomical bumps, individual monkey masks were projected to the NMT brain and averaged. For NMT surface nodes that fell within multiple ROIs across monkeys, the node was assigned to the ROI with the most monkeys. To visualize the group average ROIs, maps were threshold such that any given surface node needed to be within the ROI in three of seven monkeys. To create probabilistic functional maps of face-selective PL, ML, and AL for each monkey, the face-patch ROIs were averaged across all other monkeys.

Multielectrode Array Localization. After array implantation, CT scans (0.5 × 0.5 × 1.25 mm) were collected. Each monkey's CT image was spatially aligned to its MPRAGE anatomical image. Because brain/skull contrast is opposite between CT and MPRAGE MRI images, the two volumes were aligned by manually creating a binary brain mask for both CT and MPRAGE images and rigidly aligning the brain masks. The resulting spatial transformation matrix was applied to bring the CT and MPRAGE images into alignment. The locations of the arrays were then compared to the location of the STS bumps.

Multielectrode Array Analyses. The raw data comprised event ("spike") times per channel for the entire experimental session. To characterize tuning of each recording site, images of isolated faces, hands, bodies, and objects on a white background were presented within the activating region of all of the visually responsive sites. Each image subtended 4 ° and was presented for 100 ms ON and 200 ms OFF. Responses were defined as the mean firing rate over 80 to 250 ms after image onset minus the mean firing rate over the first 30 ms after image onset. Responses were averaged across image repetitions.

Histological Analyses. Six monkeys (M3, M19–M24) that reached end points were euthanized by intravenous injection of SomnaSol (dose of sodium pentobarbital was 120 mg/kg), and transcardially perfused by rinse (0.9% sodium chloride + 0.5% sodium nitrite) followed by 4% paraformaldehyde in 0.1 M phosphate buffer, pH 7.4. After postfixation overnight, brain was placed into 30% sucrose in 0.1 M phenobarbital. Coronal and parasagittal 50-μm sections were cut on freezing microtome. Serial sections, mounted on glass slides and postfixed for 12 d in formolsaline (10% formaline + 9 g/L sodium chloride), were stained for myelin by the Gallyas method (68). Another batch of free-floating sections was processed for cytochrome oxidase according to a standard technique (69). For Nissl staining, 0.5% water solution of thionine was used. Digital images of stained sections were captured using a Panasonic Lumix DMC-ZS7 camera with a 12× optical zoom and a light box for uniform lighting. The brightness and contrast of each image were adjusted in Photoshop using the stria of Gennari in V1 as a reference. For cytochrome sections (*SI Appendix*, Fig. S15), the darkest pixel values were extracted from each image and colored bright green using the curves function in Photoshop.

Data Availability. Data have been deposited in GitHub (https://github.com/mikearcaro/STSbumps) and Zenodo (70).

1. R. Rajimehr, R. B. Tootell, Does retinotopy influence cortical folding in primate visual cortex? *J. Neurosci.* **29**, 11149–11152 (2009).
2. S. Da Costa *et al.*, Human primary auditory cortex follows the shape of Heschl's gyrus. *J. Neurosci.* **31**, 14067–14075 (2011).
3. B. Fischl *et al.*, Cortical folding patterns and predicting cytoarchitecture. *Cereb. Cortex* **18**, 1973–1980 (2008).
4. J. H. Kaas, R. J. Nelson, M. Sur, C. S. Lin, M. M. Merzenich, Multiple representations of the body within the primary somatosensory cortex of primates. *Science* **204**, 521–523 (1979).
5. O. Hinds *et al.*, The intrinsic shape of human and macaque primary visual cortex. *Cereb. Cortex* **18**, 2586–2595 (2008).
6. G. Holmes, Disturbances of vision by cerebral lesions. *Br. J. Ophthalmol.* **2**, 353–384 (1918).

7. M. M. Schira, C. W. Tyler, M. Breakspear, B. Spehar, The foveal confluence in human visual cortex. *J. Neurosci.* **29**, 9050–9058 (2009).

8. N. C. Benson *et al.*, The retinotopic organization of striate cortex is well predicted by surface topology. *Curr. Biol.* **22**, 2081–2085 (2012).

9. N. Witthoft *et al.*, Where is human V4? Predicting the location of hV4 and VO1 from cortical folding. *Cereb. Cortex* **24**, 2401–2408 (2014).

10. F. Leroy *et al.*, New human-specific brain landmark: The depth asymmetry of superior temporal sulcus. *Proc. Natl. Acad. Sci. U.S.A.* **112**, 1208–1213 (2015).

11. K. S. Weiner *et al.*, The mid-fusiform sulcus: A landmark identifying both cytoarchitectonic and functional divisions of human ventral temporal cortex. *Neuroimage* **84**, 453–465 (2014).

12. C. Amiez, M. Petrides, Neuroimaging evidence of the anatomo-functional organization of the human cingulate motor areas. *Cereb. Cortex* **24**, 563–578 (2014).

13. N. C. Benson, O. H. Butt, D. H. Brainard, G. K. Aguirre, Correction of distortion in flattened representations of the cortical surface allows prediction of V1-V3 functional organization from anatomy. *PLOS Comput. Biol.* **10**, e1003538 (2014).

14. D. Y. Tsao, W. A. Freiwald, R. B. Tootell, M. S. Livingstone, A cortical region consisting entirely of face-selective cells. *Science* **311**, 670–674 (2006).

15. D. Y. Tsao, S. Moeller, W. A. Freiwald, Comparing face patch systems in macaques and humans. *Proc. Natl. Acad. Sci. U.S.A.* **105**, 19514–19519 (2008).

16. A. H. Bell, F. Hadj-Bouziane, J. B. Frihauf, R. B. Tootell, L. G. Ungerleider, Object representations in the temporal cortex of monkeys and humans as revealed by functional magnetic resonance imaging. *J. Neurophysiol.* **101**, 688–700 (2009).

17. M. A. Pinsk *et al.*, Neural representations of faces and body parts in macaque and human cortex: A comparative FMRI study. *J. Neurophysiol.* **101**, 2581–2600 (2009).

18. T. Janssens, Q. Zhu, I. D. Popivanov, W. Vanduffel, Probabilistic and single-subject retinotopic maps reveal the topographic organization of face patches in the macaque cortex. *J. Neurosci.* **34**, 10156–10167 (2014).

19. M. J. Arcaro, P. F. Schade, J. L. Vincent, C. R. Ponce, M. S. Livingstone, Seeing faces is necessary for face-domain formation. *Nat. Neurosci.* **20**, 1404–1412 (2017).

20. M. S. Livingstone *et al.*, Development of the macaque face-patch system. *Nat. Commun.* **8**, 14897 (2017).

21. C. J. Shatz, P. Rakic, The genesis of efferent connections from the visual cortex of the fetal rhesus monkey. *J. Comp. Neurol.* **196**, 287–307 (1981).

22. T. Ochiai *et al.*, Sulcal pattern and morphology of the superior temporal sulcus. *Neuroimage* **22**, 706–719 (2004).

23. M. K. Hasnain, P. T. Fox, M. G. Woldorff, Structure–function spatial covariance in the human visual cortex. *Cereb. Cortex* **11**, 702–716 (2001).

24. K. Grill-Spector, K. S. Weiner, The functional architecture of the ventral temporal cortex and its role in categorization. *Nat. Rev. Neurosci.* **15**, 536–548 (2014).

25. V. S. Natu *et al.*, Sulcal depth in the medial ventral temporal cortex predicts the location of a place-selective regions in macaques, children, and adults. *Cereb. Cortex*, 10.1093/cercor/bhaa203 (2020).

26. K. S. Weiner, J. D. Yeatman, "The cognitive neuroanatomy of human ventral occipitotemporal cortex" in *The Cognitive Neurosciences*, M. Gazzaniga, Ed. (MIT Press, Cambridge, MA, 2020), vol. 6, pp. 109–116.

27. V. S. Natu *et al.*, Sulcal depth in the medial ventral temporal cortex predicts the location of a place-selective region in macaques, children, and adults. *Cereb. Cortex*, 10.1093/cercor/bhaa203 (2020).

28. T. M. Preuss, P. S. Goldman-Rakic, Myelo- and cytoarchitecture of the granular frontal cortex and surrounding regions in the strepsirhine primate Galago and the anthropoid primate Macaca. *J. Comp. Neurol.* **310**, 429–474 (1991).

29. D. C. Van Essen, A tension-based theory of morphogenesis and compact wiring in the central nervous system. *Nature* **385**, 313–318 (1997).

30. X. Li *et al.*, Commonly preserved and species-specific gyral folding patterns across primate brains. *Brain Struct. Funct.* **222**, 2127–2141 (2017).

31. J. Régis *et al.*, "Sulcal root" generic model: A hypothesis to overcome the variability of the human cortex folding patterns. *Neurol. Med. Chir. (Tokyo)* **45**, 1–17 (2005).

32. B. G. Rash *et al.*, Gliogenesis in the outer subventricular zone promotes enlargement and gyrification of the primate cerebrum. *Proc. Natl. Acad. Sci. U.S.A.* **116**, 7089–7094 (2019).

33. P. Rakic, Specification of cerebral cortical areas. *Science* **241**, 170–176 (1988).

34. W. Welker, "Why does cerebral cortex fissure and fold? A review of determinants of gyri and sulci" in *Cerebral Cortex*, A. Peters, E. G. Jones, Eds. (Plenum, New York, 1990), pp. 3–136.

35. C. Bodin, S. Takerkart, P. Belin, O. Coulon, Anatomo-functional correspondence in the superior temporal sulcus. *Brain Struct. Funct.* **223**, 221–232 (2018).

36. C. Bodin *et al.*, Plis de passage in the superior temporal sulcus: Morphology and local connectivity. *Neuroimage* **225**, 117513 (2020).

37. J. F. Mangin *et al.*, "Plis de passage" deserve a role in models of the cortical folding process. *Brain Topogr.* **32**, 1035–1048 (2019).

38. P. Grimaldi, K. S. Saleem, D. Tsao, Anatomical connections of the functionally defined "face patches" in the macaque monkey. *Neuron* **90**, 1325–1342 (2016).

39. A. Cachia *et al.*, How interindividual differences in brain anatomy shape reading accuracy. *Brain Struct. Funct.* **223**, 701–712 (2018).

40. P. V. Bayly, L. A. Taber, C. D. Kroenke, Mechanical forces in cerebral cortical folding: A review of measurements and models. *J. Mech. Behav. Biomed. Mater.* **29**, 568–581 (2014).

41. D. P. Richman, R. M. Stewart, J. W. Hutchinson, V. S. Caviness Jr, Mechanical model of brain convolutional development. *Science* **189**, 18–21 (1975).

42. T. Tallinen, J. Y. Chung, J. S. Biggins, L. Mahadevan, Gyrification from constrained cortical expansion. *Proc. Natl. Acad. Sci. U.S.A.* **111**, 12667–12672 (2014).

43. J. H. Lui, D. V. Hansen, A. R. Kriegstein, Development and evolution of the human neocortex. *Cell* **146**, 18–36 (2011).

44. C. D. Kroenke, P. V. Bayly, How forces fold the cerebral cortex. *J. Neurosci.* **38**, 767–775 (2018).

45. P. L. Aparicio, E. B. Issa, J. J. DiCarlo, Neurophysiological organization of the middle face patch in macaque inferior temporal cortex. *J. Neurosci.* **36**, 12729–12745 (2016).

46. M. J. Arcaro, M. S. Livingstone, A hierarchical, retinotopic proto-organization of the primate visual system at birth. *eLife* **6**, e26196 (2017).

47. J. Gomez, V. Natu, B. Jeska, M. Barnett, K. Grill-Spector, Development differentially sculpts receptive fields across early and high-level human visual cortex. *Nat. Commun.* **9**, 788 (2018).

48. B. R. Conway, The organization and operation of inferior temporal cortex. *Annu. Rev. Vis. Sci.* **4**, 381–402 (2018).

49. E. Premereur, J. Taubert, P. Janssen, R. Vogels, W. Vanduffel, Effective connectivity reveals largely independent parallel networks of face and body patches. *Curr. Biol.* **26**, 3269–3279 (2016).

50. I. D. Popivanov, J. Jastorff, W. Vanduffel, R. Vogels, Stimulus representations in body-selective regions of the macaque cortex assessed with event-related fMRI. *Neuroimage* **63**, 723–741 (2012).

51. R. Lafer-Sousa, B. R. Conway, Parallel, multi-stage processing of colors, faces and shapes in macaque inferior temporal cortex. *Nat. Neurosci.* **16**, 1870–1878 (2013).

52. C. C. Hilgetag, H. Barbas, Developmental mechanics of the primate cerebral cortex. *Anat. Embryol. (Berl.)* **210**, 411–417 (2005).

53. F. Mortazavi, S. E. Romano, D. L. Rosene, K. S. Rockland, A survey of white matter neurons at the gyral crowns and sulcal depths in the rhesus monkey. *Front. Neuroanat.* **11**, 69 (2017).

54. C. C. Hilgetag, H. Barbas, Role of mechanical factors in the morphology of the primate cerebral cortex. *PLOS Comput. Biol.* **2**, e22 (2006).

55. D. Pitcher, S. Japee, L. Rauth, L. G. Ungerleider, The superior temporal sulcus is causally connected to the amygdala: A combined TBS-fMRI study. *J. Neurosci.* **37**, 1156–1161 (2017).

56. B. Deen, K. Koldewyn, N. Kanwisher, R. Saxe, Functional organization of social perception and cognition in the superior temporal sulcus. *Cereb. Cortex* **25**, 4596–4609 (2015).

57. M. J. Arcaro, M. S. Livingstone, Retinotopic organization of scene areas in macaque inferior temporal cortex. *J. Neurosci.* **37**, 7373–7389 (2017).

58. D. B. McMahon, I. V. Bondar, O. A. Afuwape, D. C. Ide, D. A. Leopold, One month in the life of a neuron: Longitudinal single-unit electrophysiology in the monkey visual system. *J. Neurophysiol.* **112**, 1748–1762 (2014).

59. B. Fischl, A. M. Dale, Measuring the thickness of the human cerebral cortex from magnetic resonance images. *Proc. Natl. Acad. Sci. U.S.A.* **97**, 11050–11055 (2000).

60. V. Willenbockel *et al.*, The SHINE toolbox for controlling low-level image properties. *J. Vis.* **10**, 653 (2010).

61. F. P. Leite *et al.*, Repeated fMRI using iron oxide contrast agent in awake, behaving macaques at 3 Tesla. *Neuroimage* **16**, 283–294 (2002).

62. W. Vanduffel *et al.*, Visual motion processing investigated using contrast agent-enhanced fMRI in awake behaving monkeys. *Neuron* **32**, 565–577 (2001).

63. R. W. Cox, AFNI: Software for analysis and visualization of functional magnetic resonance neuroimages. *Comput. Biomed. Res.* **29**, 162–173 (1996).

64. Z. S. Saad, R. C. Reynolds, Suma. *Neuroimage* **62**, 768–773 (2012).

65. A. M. Dale, B. Fischl, M. I. Sereno, Cortical surface-based analysis. I. Segmentation and surface reconstruction. *Neuroimage* **9**, 179–194 (1999).

66. B. Fischl, M. I. Sereno, A. M. Dale, Cortical surface-based analysis. II: Inflation, flattening, and a surface-based coordinate system. *Neuroimage* **9**, 195–207 (1999).

67. J. Mandeville, JIP fMRI analysis toolkit. https://www.nitrc.org/projects/jip. Accessed 24 November 2020.

68. F. Gallyas, Silver staining of myelin by means of physical development. *Neurol. Res.* **1**, 203–209 (1979).

69. M. Wong-Riley, Columnar cortico-cortical interconnections within the visual system of the squirrel and macaque monkeys. *Brain Res.* **162**, 201–217 (1979).

70. M. Arcaro, mikearcaro/STSbumps: Data from Arcaro et al. 2020 PNAS (Version v1.0.0). *Zenodo.* http://doi.org/10.5281/zenodo.4279879. Deposited 18 November 2020.